JACS
JOURNAL OF THE AMERICAN CHEMICAL SOCIETY

Solid-State Characterization and Photoinduced Intramolecular Electron Transfer in a Nanoconfined Octacationic Homo[2]Catenane

Jonathan C. Barnes,[†,⊥] Marco Frasconi,[†] Ryan M. Young,[†,₪] Nezar H. Khdary,[±] Wei-Guang Liu,[§] Scott M. Dyar,[†] Paul R. McGonigal,[†] Ian C. Gibbs-Hall,[†] Christian S. Diercks,[†] Amy A. Sarjeant,[†] Charlotte L. Stern,[†] William A. Goddard, III,[§] Michael R. Wasielewski,[†,₪] J. Fraser Stoddart[†,*]

[†]Department of Chemistry and [₪]Argonne-Northwestern Solar Energy Research (ANSER) Center Northwestern University, 2145 Sheridan Road, Evanston, Illinois 60208, United States

[§]Materials and Process Simulation Center, California Institute of Technology, 1200 East California Boulevard, Pasadena, California 91125, United States

[±]National Center for Nano Technology Research, King Abdulaziz City for Science and Technology (KACST) P.O. Box 6086, Riyadh 11442, Kingdom of Saudi Arabia

[⊥]Department of Chemistry, Massachusetts Institute of Technology, 77 Massachusetts Avenue, Cambridge, Massachusetts 02139, United States

Supplementary Information

Table of Contents

Section A. Materials / General Methods / Instrumentation

All reagents were purchased from commercial suppliers (Aldrich or Fisher) and used without further purification. UV/Vis/NIR absorbance spectra were recorded using a UV-3600 Shimadzu spectrophotometer. Nuclear magnetic resonance (NMR) spectra were recorded on a BrukerAvance 500 spectrometer, with working frequency of 500 MHz. Chemical shifts are reported in ppm relative to the signals corresponding to the residual non-deuterated solvents (CD_3CN: δ_H = 1.94 ppm and δ_C = 118.36 ppm). **HC**•$7PF_6$ was synthesized as reported[S1] previously and purified using preparative reverse-phase high-performance liquid chromatography (RP-HPLC) on a C_{18} column employing a binary solvent system (MeCN and H_2O with 0.1% CF_3CO_2H). Further purification of **HC**•$7PF_6$ was carried out, if required, by employing a 2% NH_4PF_6 in Me_2CO mobile phase on a preparative thin-layer chromatography (TLC) silica stationary phase (20 x 20, 1500 microns) obtained from Analtech, Inc.

Visible/near-infrared femtosecond transient absorption spectroscopy was performed on an instrument described in detail elsewhere.[S2] Briefly, the 827 nm fundamental output of a commercial Ti:sapphire laser system (Tsunami oscillator / Spitfire amplifier, Spectra-Physics) split into a pump and a probe beam. For the 275 nm pump, a third-harmonic generator (THG) was constructed by first using a 1:2 telescope to reduce the diameter of the fundamental to ~1.5 mm and then frequency-doubling in a lithium triborate (LBO, θ = 90°, ϕ = 31.7°, 1 mm) crystal. The fundamental and the second harmonic at 414 nm were separated using a 400 nm high-reflecting mirror (high transmission at 800 nm). The transmitted fundamental was directed through a waveplate to rotate its polarization to be parallel to the 414 nm beam. Each beam was made to travel the same optical length: the second harmonic was directed onto a manual delay stage to match the transit times of the two beams prior to recombination. The beams were recombined with an 800 nm high-reflecting mirror (high transmission at 400 nm) and together directed into a sum-frequency generating β-barium borate crystal (BBO, θ = 40.5°, ϕ = 0°). The generated third harmonic at 275 nm was isolated using multiple 266 nm high-reflecting mirrors.

For the visible (535 nm) pump, the THG is bypassed and the majority of the laser fundamental is instead frequency doubled to 414 nm (~150 μJ/pulse) and used to pump a seeded, two-stage,

laboratory-constructed optical parametric amplifier (OPA). The 535 nm signal beam was isolated as the pump. In either case, the pump beam is routed through an optomechanical chopper operating at 500 Hz. Pump and probe beams were polarized to 54.7º relative to each other to suppress the effects of rotational dynamics.

Transient absorption signals were detected using a customized Helios system (Ultrafast Systems, LLC). As a result of the large group-velocity mismatch (GVM) between the ultraviolet pump and continuum probe in the 2 mm quartz cuvettes, the time resolution of the instrument is limited to ~1 ps, obscuring dynamics in the earliest times;[S3] no attempt has been made, however, at inferring anything during this time range in these experiments. Samples were stirred during the measurement to reduce the effects of local heating by the ultraviolet pump. The pulse energy of the 275 nm pump was reduced to ~200–300 nJ/pulse in order to avoid photoionization of the solvent and the production of solvated electrons.[S4]

Transient absorption data were first corrected for scattered light and group delay dispersion (GDD, or "chirp") using Surface Xplorer Pro 2.2.3 (Ultrafast Systems, LLC). Global fitting was accomplished in Surface Xplorer by fitting the (at most three) principle components determined using Singular Value Decomposition (SVD) to a sum of exponentials convoluted with a Gaussian instrument response function.

EPR Measurements at X-band (9.5 GHz) were carried out at room temperature using a Bruker Elexsys E580-X EPR spectrometer outfitted with a variable Q dielectric resonator (ER-4118X-MD5-W1). After the structure of **HC**•8SbF_6 had been confirmed by X-ray diffraction analysis, the single crystals were loaded into quartz 1.4 mm tubes and sealed with a clear ridged UV doming epoxy (IllumaBond 60-7160RCL). All samples were used immediately after preparation. Steady-state CW EPR spectra were measured at X-band using 2 mW microwave power and 0.1 G field modulation at 100 KHz, with a time constant of 10.24 ms and a conversion time of 40.96 ms.

B. Synthetic Protocols

Chemical Oxidation of HC•7PF$_6$ to HC•8SbF$_6$

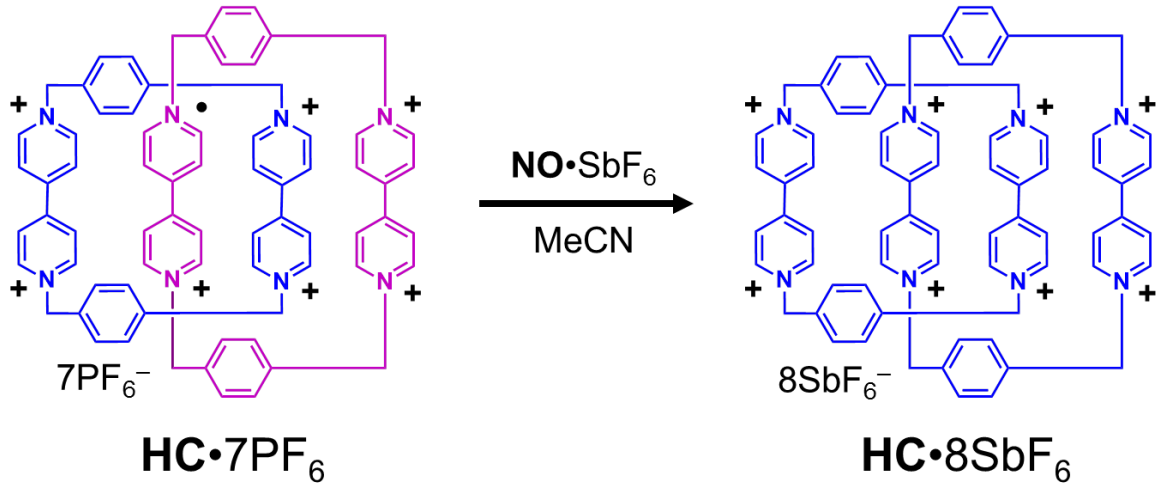

Scheme S1. Chemical oxidation of **HC**•7PF$_6$ to **HC**•8SbF$_6$ using excess of **NO**•SbF$_6$.

HC•8SbF$_6$: **HC**•7PF$_6$ (8.2 mg, 3.99 μmol) was dissolved in dry MeCN (2 mL), followed by the addition of **NO**•SbF$_6$ (10.6 mg, 39.9 μmol, 10 equiv), resulting in a change in the color of the solution from dark purple to pale yellow as a consequence of complete oxidation to the octacationic **HC**•8SbF$_6$ (quantitative). ^{1}H NMR (500 MHz, CD$_3$CN): δ_H 8.97 (d, J = 6.9 Hz, 8H), 8.80 (d, J = 6.9 Hz, 8H), 8.22 (d, J = 8.3 Hz, 8H), 8.10 (d, J = 8.3 Hz, 8H), 7.69 (d, J = 6.9 Hz, 8H), 6.10 (s, 8H), 5.97 (s, 8H), 4.18 (d, J = 6.8 Hz, 8H). ^{13}C NMR (125 MHz, CD$_3$CN): δ_C 147.4, 147.1, 145.5, 141.9, 138.8, 137.0, 131.5, 130.9, 126.9, 121.2, 65.7, 64.0.

Section C. Crystallographic Characterization

All crystallographic data are available free of charge from the Cambridge Crystallographic Data Centre (CCDC) via www.ccdc.cam.ac.uk/data_request/cif.

1) HC•8SbF$_6$

a) Methods. **HC**•7PF$_6$ (12.3 mg, 6.0 μmol) was dissolved in MeCN (2.0 mL, 3 mM solution), followed by the addition of **NO**•SbF$_6$ (16.0 mg, 60.0 μmol). The addition of the oxidant led to an immediate change in the color of the solution from dark purple to pale yellow. Single crystals

were grown by layer-by-layer diffusion of iPr$_2$O into an oxidized 3 mM MeCN solution of **HC**•8SbF$_6$ inside a capped 538 Wilmad NMR tube. After approximately one week of diffusion, single crystals (Figure S1) of **HC**•8SbF$_6$ were obtained that were suitable for X-ray diffraction. Data were collected at 100 K on a Bruker APEX-II CCD Diffractometer equipped with a CuK$_\alpha$ microsource with Quazar optics.

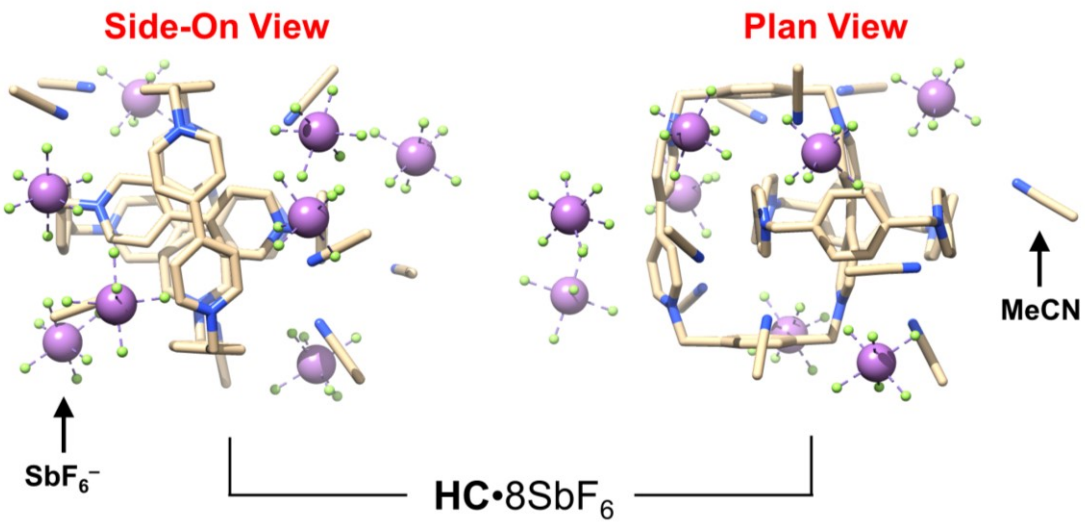

Figure S1. Different crystallographic views of the solid-state structure of **HC**•8SbF$_6$. Counterions (SbF_6^-) and solvent molecules (MeCN) are included to demonstrate how the charge-screening SbF_6^- ions surround the [2]catenane.

b) Crystal Parameters. ($C_{72}H_{64}N_8F_{48}Sb_8$)•9($C_2H_3N$) ($M$ =3296.79): triclinic, space group $P\bar{1}$ (no. 2), a = 16.4947(7), b = 16.7464(7), c = 22.8838(10) Å, α = 86.675(2), β = 78.450(2), γ = 71.512(2)°, V = 5873.4(4) Å^3, Z = 2, T = 100(2) K, μ(CuKα) = 15.493 mm^{-1}, ρ_{calc} = 1.864 g/mm^3, 79636 reflections measured ($3.94 \leq 2\Theta \leq 136.622$), 21245 unique ($R_{int}$ = 0.0760, R_{sigma} = 0.0686) which were used in all calculations. The final R_1 was 0.0886 ($I > 2\sigma(I)$) and wR_2 was 0.2552 (all data). Using Olex2[S5], the structure was solved with the ShelXD[S6]structure solution program using Dual Space and refined with the ShelXL[S6] refinement package using Least Squares minimization. The enhanced rigid bond restraint (RIGU) was applied globally. The solvent masking procedure as implemented in Olex2 was used to remove the electronic contribution of disordered and partially occupied acetonitrile solvent molecules from the refinement. Total solvent accessible volume / cell = 341.5 Å^3 [5.8%]. Total electron count / cell = 95.1. CCDC number: 998871.

Section D. Spectroscopic Characterization

1) ^{1}H NMR / ^{13}C NMR Spectroscopic Analysis of HC•8SbF$_6$

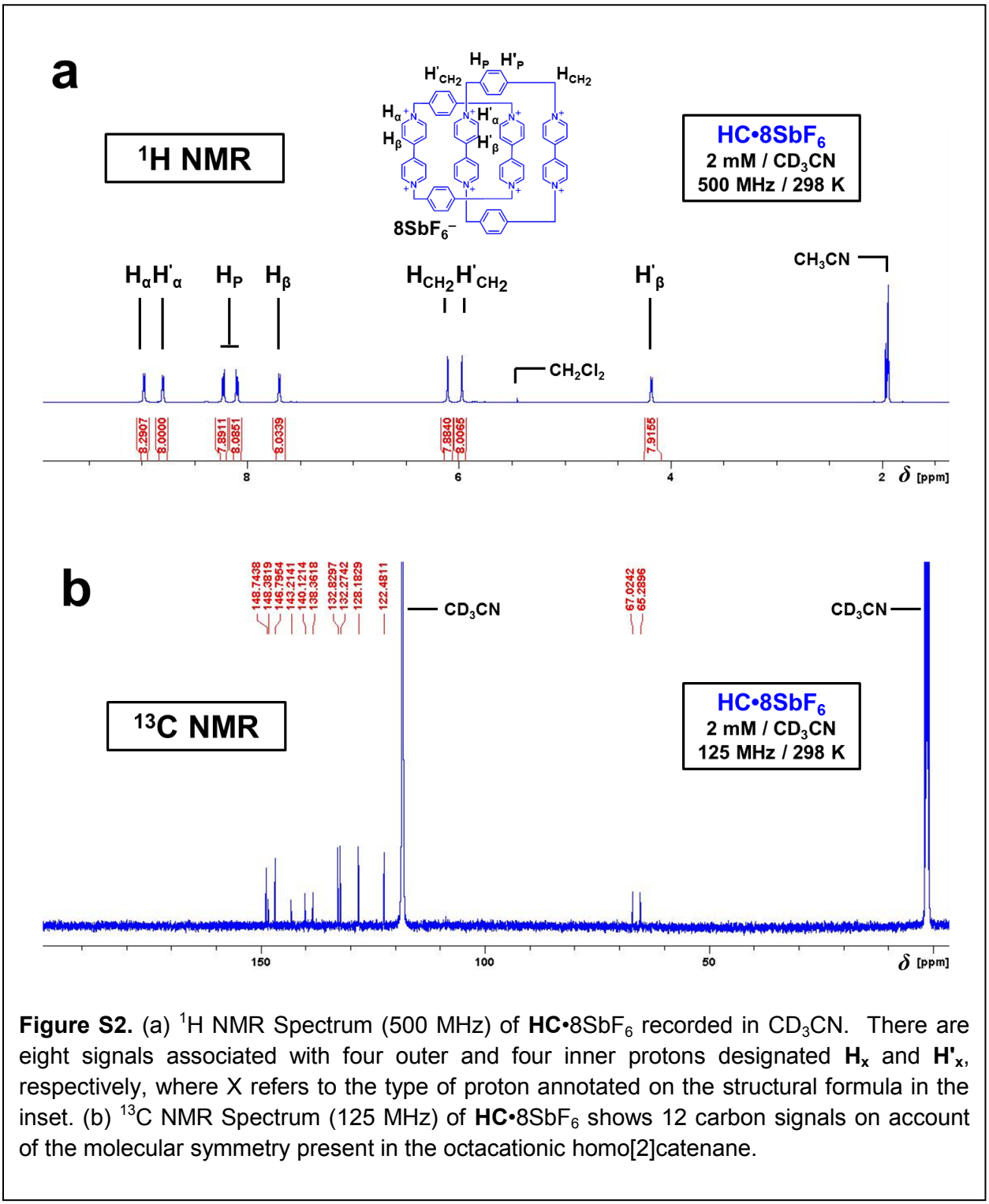

Figure S2. (a) ^{1}H NMR Spectrum (500 MHz) of **HC**•8SbF$_6$ recorded in CD$_3$CN. There are eight signals associated with four outer and four inner protons designated $\mathbf{H_x}$ and $\mathbf{H'_x}$, respectively, where X refers to the type of proton annotated on the structural formula in the inset. (b) ^{13}C NMR Spectrum (125 MHz) of **HC**•8SbF$_6$ shows 12 carbon signals on account of the molecular symmetry present in the octacationic homo[2]catenane.

2) Femtosecond Transient Absorption Spectroscopy

a) HC•7PF$_6$

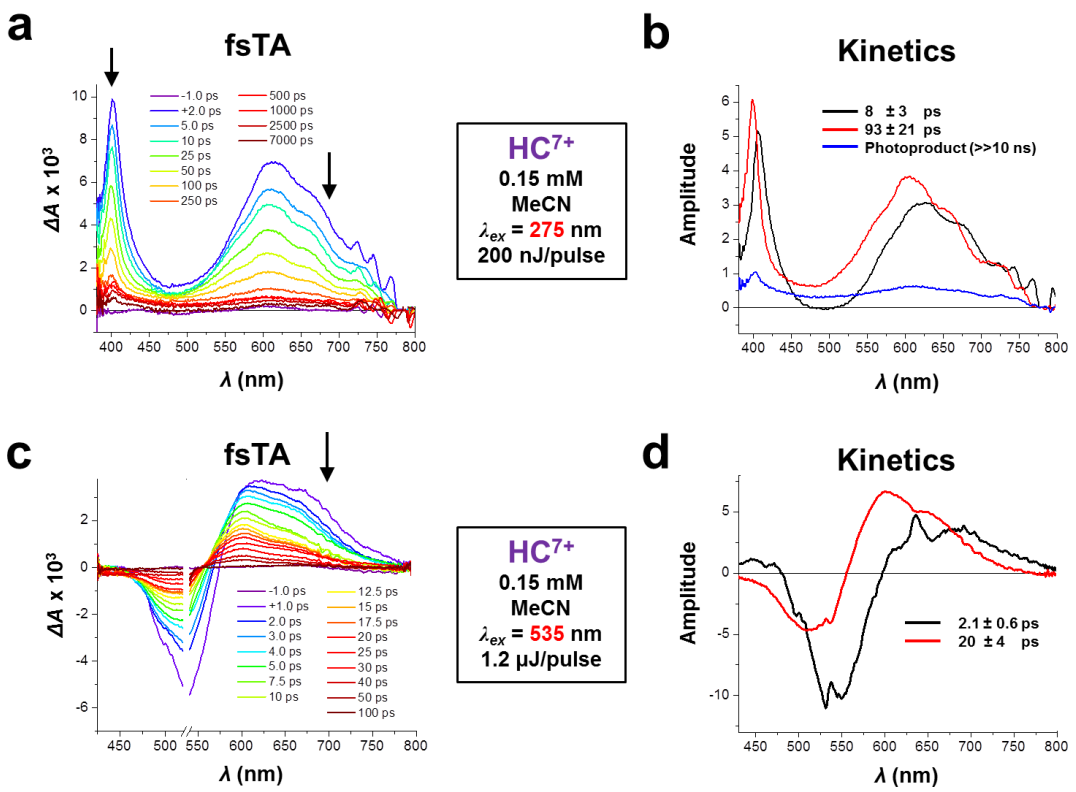

Figure S3. Femtosecond transient absorption spectra (fsTA) for **HC**•7PF$_6$. (a) Excitation at 275 nm and (c) 535 nm, along with the corresponding (b and d) kinetic plots.

Although samples were stirred, and excited at low power to avoid accumulation of photo-generated decomposition products, some byproducts may be accumulating that absorb on the blue edge. Electron transfer after excitation at 275 nm (Figure S3a) appears to occur within ~8 ps, according to the global fit, with the initially populated component (black) resembling the spectrum of **MV**$^{*2+}$, followed by blue-shifting to generate a spectrum (red) more similar to the viologen radical cation. The charges then recombine (Figure S3b) in 95 ± 2 ps. The fact that the absorption maximum beyond 500 nm occurs at 611 nm, in combination with the similarity of the spectral lineshapes, suggests that **HC**$^{7+}$ follows a similar electron-transfer pathway (Figure 4) as **HC**$^{8+}$. Excitation at 535 nm (Figure S3c), however, generates a broader absorption band that blue-shifts to 611 nm in ~2 ps (Figure S3d), a transition which suggests that the initial irradiation excites the unpaired electron that resides in the SOMO leading to gradual charge recombination

and a spectral lineshape reminiscent of the diagnostic viologen radical cation absorption band maximized at 611 nm. This assignment is also supported by the lack of ground state bleach in the fsTA spectra near 535 nm when exciting at 275 nm. The shape of the spectrum, however, may be obfuscated by the presence of the ground-state bleach in the 480–600 nm region, and so correlation with the viologen cation is less obvious. The lifetime (20 ps) of the transient signal is brief and unlikely to be attributable to the excited state decay but is more likely a result of rapid charge recombination. Further investigations are underway to understand fully this electron-transfer mechanism. In each of these spectra, the final principle component (blue) represents a species with a lifetime far longer than the ~7 ns experimental time window – and are assigned to photoproducts in all cases.

b) ***CBPQT•4PF$_6$***

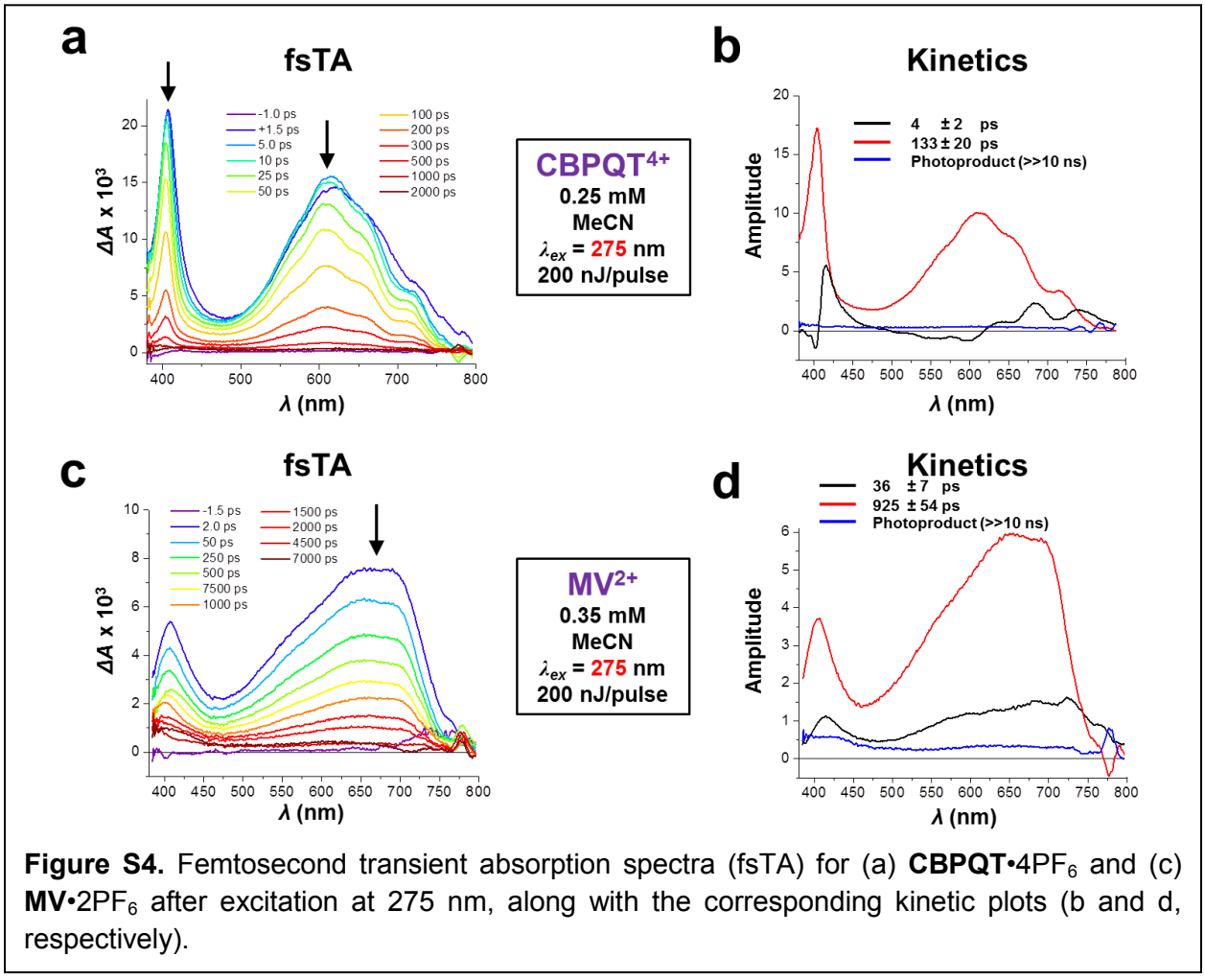

Figure S4. Femtosecond transient absorption spectra (fsTA) for (a) **CBPQT•**4PF$_6$ and (c) **MV•**2PF$_6$ after excitation at 275 nm, along with the corresponding kinetic plots (b and d, respectively).

Samples (i.e., **CBPQT**•$4PF_6$) were stirred, and excited (Figure S4a) at low power to avoid accumulation of photo-generated decomposition products. Global analysis (Figure S4b) shows that within ~4 ps of the excitation, the first principle spectrum (black curve) shows a fast decay of the features near ~750 nm and a rise of those near ~600 nm, ultimately resulting in a shift in the transient absorption spectrum. We attribute this ~4 ps shift to charge separation, where an electron on one of the paraphenylene rings is transferred to one of the viologen subunits in $\mathbf{CBPQT^{4+}}$. At times > 5 ps (Figure S4b, red principle spectrum), the spectra all strongly resemble that of the viologen radical cation, i.e., absorption at 611 nm, along with similar vibronic character on the red side. The charges subsequently recombine in ~135 ps on a similar timescale as **HC**•$8SbF_6$. All of the charge separation and recombination timescales for $\mathbf{CBPQT^{4+}}$, $\mathbf{HC^{7+}}$, and $\mathbf{HC^{8+}}$ are summarized in Table S1, where the time constants are taken as the average of the values extracted from the fits and errors as the standard deviation over multiple experiments.

Table S1. **Average Charge Separation (CS) and Charge Recombination (CR) Times for $\mathbf{CBPQT^{4+}}$, $\mathbf{HC^{7+}}$ and $\mathbf{HC^{8+}}$**

	τ_{CS} (ps)	τ_{CR} (ps)
$\mathbf{CBPQT^{4+}}$	5.6 ± 1.6	130 ± 30
$\mathbf{HC^{7+}}$ (λ_{ex} = 275 nm)	8.0 ± 0.1	95 ± 2
$\mathbf{HC^{7+}}$ (λ_{ex} = 535 nm)	2.1 ± 0.6	20 ± 4
$\mathbf{HC^{8+}}$	13 ± 2	97 ± 4

*c) **MV•2PF$_6$***

Excitation of $\mathbf{MV^{2+}}$ (π–π^* transition) at 275 nm leads (Figure S4c) to the S_1–S_n* transition (populating the S_1 state), which ultimately decays biexponentially (33 ± 6 ps, 870 ± 25 ps). The longer ~870 ps component (Figure S4d) is more likely the radiative decay time. The shorter component is presumably a consequence of vibrational cooling or possibly an artifact of the

instrument as a consequence of imperfect relative polarization of the pump and probe. It is important to note that the maximum absorption wavelength for this transition is red-shifted to 687 nm and the spectral line shape is much broader than the maximum absorption band observed for $\mathbf{HC}^{8+}$ (Figure 4), $\mathbf{HC}^{7+}$ (Figure S3a), and $\mathbf{CBPQT}^{4+}$ (Figure S4a). Moreover, the relaxation time is nearly an order of magnitude longer than those electron-transfer processes, an indication which supports the mechanism of electron transfer initiating from the paraphenylene rings in $\mathbf{HC}^{8+}$, $\mathbf{HC}^{7+}$, and $\mathbf{CBPQT}^{4+}$, and not from one of the viologen subunits.

2) Electron Paramagnetic Resonance Spectroscopic Analysis of HC•8SbF$_6$

Solid-state electron paramagnetic resonance (EPR) spectroscopic analysis was carried out (Figure S5) on single crystals of **HC**•8SbF$_6$ in order to confirm complete oxidation to the octacationic redox state. The absence of a strong signal in this EPR analysis corroborates the data obtained by X-ray diffraction and also by NMR and UV/Vis/NIR spectroscopies.

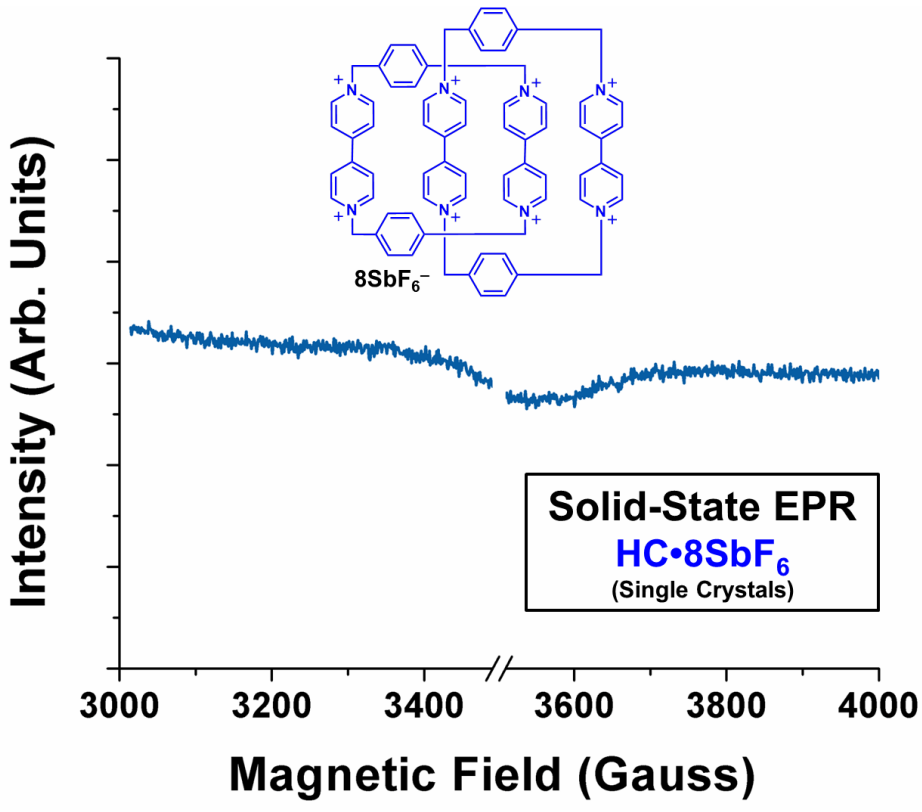

Figure S5. Solid-state EPR spectrum of **HC**•8SbF$_6$ single crystals.

Section E. Theoretical Calculations

Absorption Energies and HOMO / LUMO Depictions of HC^{8+}, HC^{7+}, $CBPQT^{3+}$, and MV^{+}

The geometries of **HC^{8+}**, **HC^{7+}**, **$CBPQT^{3+}$**, and **MV^{+}** were optimized at the level of M06[S7]/6-31G** in the Poisson-Boltzmann solvation model[S8] for acetonitrile (ε=37.5 and R_0= 2.18 Å) with Jaguar 7.7[S9]. Based on these geometries, we calculated vertical absorption energies with the time-dependent DFT (TD-DFT) method at the BLYP[S10,S11]/6-31G level with long range correction[S12] carried out by GAMESS.[S13] For closed-shell species, we used the polarizable continuum model[S14] (PCM) with the same acetonitrile radius and dielectric constant to determine the solvation effect. The transitions with oscillator strength greater than 0.01 are listed in Table S2 while the corresponding orbitals for **HC^{8+}**, **HC^{7+}**, **$CBPQT^{4+}$** and **MV^{2+}** are given in Figure S6, S7, S8 and S9, respectively.

In **HC^{8+}**, the HOMO (Figure S6) has B_2 symmetry, composed of E-like orbitals distributed over four paraphenylene rings. For the 275 nm excitation, we find a one-electron transfer to the LUMO centered at the viologen dimer $(V_2)^{4+}$ to form a mixed-valence dimer $(V_2)^{\bullet 3+}$, that we assume relaxes back to the ground state through charge recombination. Since this mixed-valence excited state S_1 of **HC^{8+}** and the ground state of **HC^{7+}** share the same HOMO under Koopmans' theorem, we calculated the excitations from the ground state of **HC^{7+}** in order to determine the nature of the transient absorption transition observed in the pump-probe experiment.

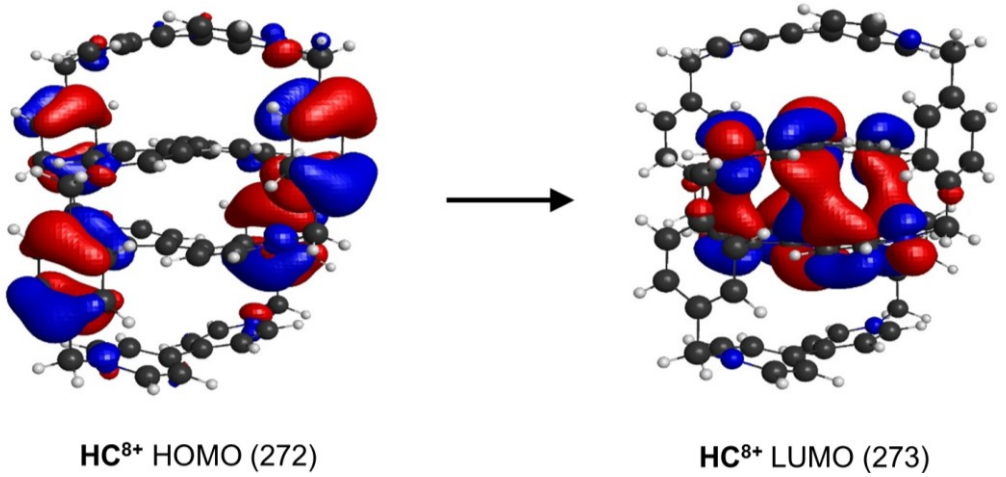

Figure S6. Orbital depictions of the **HC^{8+}** HOMO and LUMO.

Similarly, excitations from the ground state of **CBPQT**$^{3+}$ and **MV**$^{+}$ are calculated to study the transient absorption of **CBPQT***$^{4+}$ and **MV***$^{2+}$. These ground state models provide qualitatively correct results as long as the excitation does not involve the orbital filled with the extra electron. This condition is satisfied for **HC***$^{8+}$ and **CBPQT***$^{4+}$, in which the hole orbital (i.e., MO272 for **HC***$^{8+}$ and MO134 for **CBPQT***$^{4+}$) plays a small role in the excitations of interest in this investigation (see Table S2), but only marginally satisfied for **MV***$^{2+}$, as the second excited state of **MV**$^{+}$ involves the electron in MO49, which is the orbital of hole in **MV***$^{2+}$.

The lowest energy absorption (Figure 2c) of **HC**$^{7+}$ corresponds to a transition from the binding state of the middle V_2 dimer to the antibonding state of this mixed-valence state (Figure S7, MO273 to 274). The transition energy from TD-DFT is 2431 nm, but the energy difference between ground states with A and B symmetry in PCM model at m06/6-311++G** level is 1884 nm, which is in reasonable agreement with the experimental result of ~ 1415 nm observed in the UV-Vis-NIR absorption spectrum (Figure 2c) of the ground state **HC**$^{7+}$.

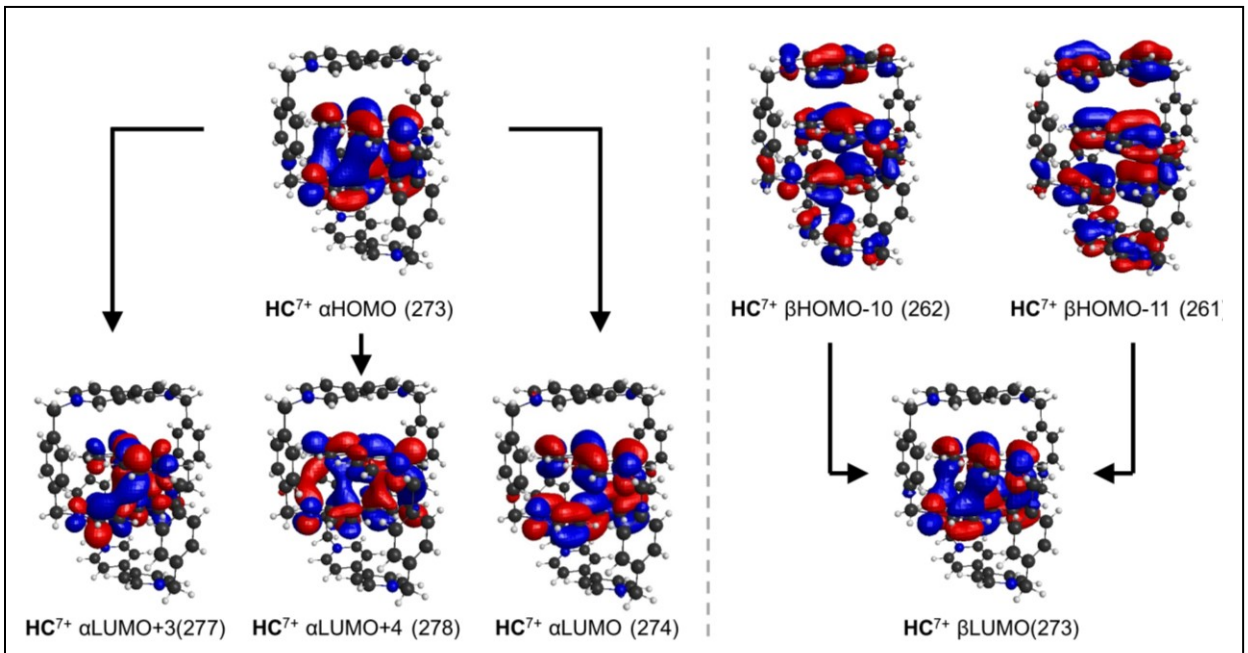

Figure S7. Orbital depictions of **HC**$^{7+}$.

The second lowest energy absorption (Figure 2c) of $\mathbf{HC}^{7+}$ corresponds to two symmetry-allowed transitions at 458 and 456 nm of the up-spin HOMO to a linear combination of the π–π* transition on two viologens. We assign this π–π* transition mode to the 600 nm peak in absorption spectrum of $\mathbf{HC}^{*8+}$ (Figure 3), which is also observed at 524 nm for $\mathbf{CBPQT}^{3+}$ and 508 nm for $\mathbf{MV}^{+}$ with similar orbital nodal structures and energies, as shown in Figure S8 and S9, respectively. Experimentally, the pump-probe spectra (Figure S4c) of $\mathbf{MV}^{2+}$ in the region of 500–700 nm is substantially different than the spectra of $\mathbf{CBPQT}^{4+}$ (Figure S4a) and $\mathbf{HC}^{8+}$ (Figure 3). This difference can be explained from the fact that the extra electron comes from MO49 (Figure S9) of the same viologen unit in $\mathbf{MV}^{2+}$, which changes the electronic Hamiltonian much more than in the case of $\mathbf{CBPQT}^{4+}$ and $\mathbf{HC}^{8+}$, where the extra electron comes from one of the nearby paraphenylene rings (see orbital depictions in Figures S8 and S6, respectively).

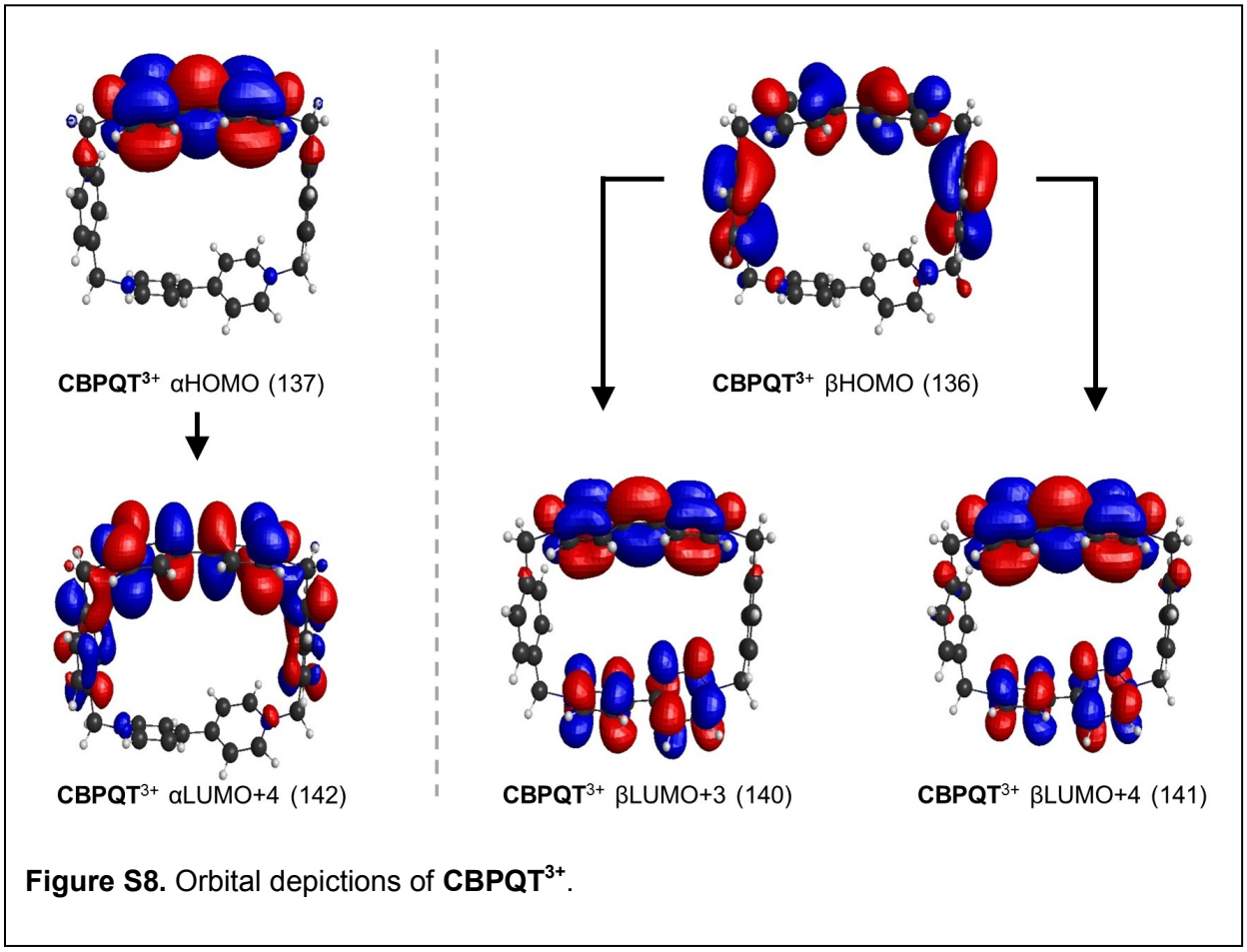

Figure S8. Orbital depictions of $\mathbf{CBPQT}^{3+}$.

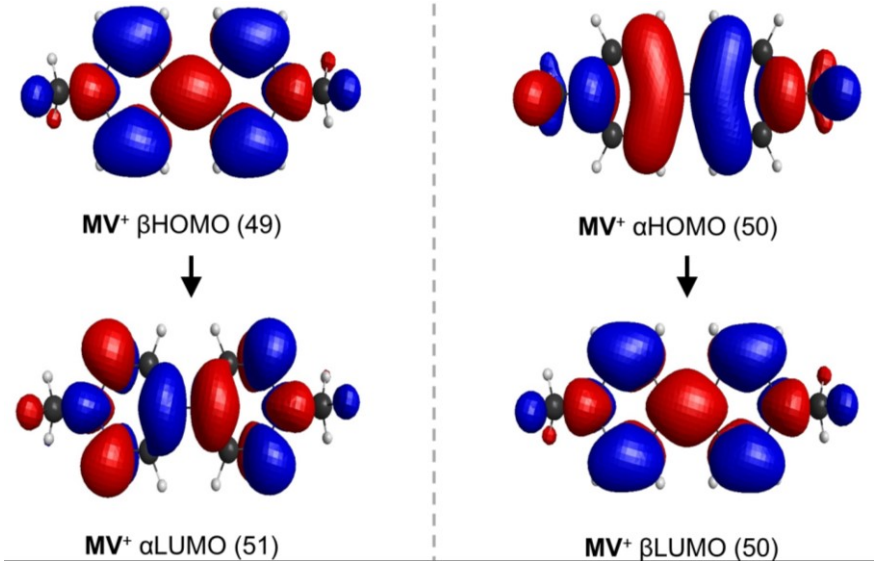

Figure S9. Orbital depictions of MV^{+}.

Table S2. Vertical Absorption Energies and Oscillator Strengths for HC^{8+}, HC^{7+}, $CBPQT^{4+}$, and MV^{2+}

	Excitation Wavelength (nm)	Main Excitation (Amplitude)	Oscillator Strength
HC^{8+} (in MeCN)	293	272→273 (-0.92)	0.020
HC^{8+} (gas phase)	327	272→273 (0.96)	0.004*
HC^{7+} (gas phase)	2431	α 273→274 (-1.02)	0.052
	458	α 273→277 (0.81)	0.098
	456	α 273→278 (0.78)	0.099
	374	β 262→273 (0.40)	0.029
	374	β 261→273 (-0.41)	0.030
$CBPQT^{4+}$ (gas phase)**	292	134→137(0.87)	0.140
$CBPQT^{3+}$ (gas phase)	524	α 137→142 (0.91)	0.356
	328	β 136→140 (0.67) β 136→141 (0.54)	0.347
MV^{2+} (gas phase)**	264	49→50(-0.98)	0.785
MV^{+} (gas phase)	508	α 50→51 (-0.94)	0.332
	321	β 49→50 (0.89)	0.468

*The largest oscillator strength among the 6 excited states calculated

**The molecular geometry is taken from the same molecule optimized with one extra electron. Only S_1 state is listed.

The third lowest energy absorption (Figure 2c) of $\mathbf{HC}^{7+}$ corresponds to two symmetry-allowed transitions of the down spin HOMO, to a linear combination of the other π–π* transition mode on two viologens, both at 374nm, which can be more clearly seen in Figure S8 and S9. We assign this transition to the 400nm peak in absorption spectra of $\mathbf{HC}^{*8+}$ (Figure 3), $\mathbf{CBPQT}^{*4+}$ (Figure S4a) and possibly $\mathbf{MV}^{*2+}$ (Figure S4c).

All of the vertical absorption energies and the corresponding oscillator strengths are summarized in Table S2.

Section D. References

S1 Barnes, J. C.; Fahrenbach, A. C.; Cao, D.; Dyar, S. M.; Frasconi, M.; Giesener, M. A.; Benítez, D.; Tkatchouk, E.; Chernyashevskyy, O.; Shin, W.-H.; Li, H.; Sampath, S.; Stern, C.L.; Sarjeant, A. A.; Hartlieb, K. J.; Liu, Z.; Carmieli, R.; Botros, Y. Y.; Choi, J. W.; Slawin, A. M. Z.; Ketterson, J. B.; Wasielewski, M. R.; Goddard III, W. A.; Stoddart, J. F. *Science* **2013**, *339*, 429–433.

S2 Young, R. M.; Dyar, S. M.; Barnes, J. C.; Juríček, M.; Stoddart, J. F.; Co, D. T.; Wasielewski, M. R. *J. Phys. Chem. A* **2013**, *117*, 12438–12448.

S3 Kozma, I. Z.; Krok, P.; Riedle, E. *J. Opt. Soc. Am. B* **2005**, *22*, 1479–1485.

S4 Peon, J.; Tan, X.; Hoerner, J. D.; Xia, C.; Luk, Y.-F.; Kohler, B. *J. Phys. Chem. A* **2001**, *105*, 5768–5777.

S5 Dolomanov, O. V.; Bourhis, L. J.; Gildea, R. J.; Howard, J. A. K.; Puschmann, H. *J. Appl. Cryst*. **2009**, *42*, 339–341.

S6 Sheldrick, G.M. *Acta Cryst.* **2008**, *A64*, 112–122.

S7 Zhao, Y.; Truhlar, D. G. *Theor. Chem. Acc.* **2008,** *120*, 215–241.

S8 Tannor, D. J.; Marten, B.; Murphy, R.; Friesner, R. A.; Sitkoff, D.; Nicholls, A.; Ringnalda, M.; Goddard, W. A.; Honig, B. *J. Am. Chem. Soc.* **1994**, *116*, 11875–11882.

S9 Jaguar, *Schrodinger, LLC, New York, NY* **2007**.

S10 Becke, A. D. *Phys. Rev. A* **1988**, *38*, 3098–3100.

S11 Lee, C. T.; Yang, W. T.; Parr, R. G. *Phys. Rev. B* **1988**, *37*, 785–789.

S12 Iikura, H.; Tsuneda, T.; Yanai, T.; Hirao, K. *J. Chem. Phys.* **2001**, *115*, 3540–3544.

S13 Schmidt, M. W.; Baldridge, K. K.; Boatz, J. A.; Elbert, S. T.; Gordon, M. S.; Jensen, J. H.; Koseki, S.; Matsunaga, N.; Nguyen, K. A.; Su, S. J.; Windus, T. L.; Dupuis, M.; Montgomery, J. A. *J. Comput. Chem.* **1993**, *14*, 1347–1363.

S14 Cossi, M.; Barone, V. *J. Chem. Phys.* **2000**, *112*, 2427–2435.